

Enthalpy-Driven Self-Healing in Thin Metallic Films on Flexible Substrates

Claus Othmar Wolfgang Trost,* Alice Lassnig, Patrice Kreiml, Tanja Jörg, Velislava L. Terziyska, Christian. Mitterer, and Megan Jo Cordill*

Self-healing microelectronics are needed for costly applications with limited or without access. They are needed in fields such as space exploration to increase lifetime and decrease both costs and the environmental impact. While advanced self-healing mechanisms for polymers are numerous, practical ways for self-healing in metal films have yet to be found. A concept for an autonomous intrinsic self-healing metallic film system is developed, allowing the healing of cracks in metallic films on flexible substrates. The concept relies on stabilizing metastable thin films with high mixing enthalpy via segregation barriers. This allows the films to possess autonomous intrinsic self-healing capabilities triggered by cracking at temperatures not detrimental to flexible microelectronics. The effect will be shown on metastable $\text{Mo}_{1-x}\text{Ag}_x$ thin films, stabilized via a Mo segregation barrier. Without a segregation barrier, the system is known to exhibit spontaneous Ag particle formation on the surface. This property is controlled and directed to heal cracks and partially restore the electro-mechanical properties of the multilayer system. This mechanism opens up the field of self-healing thin metallic films that could profoundly impact the design of future microelectronics.

1. Introduction

Organic materials, such as tissue or bones, are capable of healing. In contrast, engineering materials usually lack the property to detect and repair failures, such as cracks. Therefore, engineering safety factors are still needed in the design stage to prevent fatal failure. Additionally, not alternatively, to the damage prevention principle, the damage management principle^[1] can be used. Damage management has been used for centuries. Seymour et al.^[2] showed that Roman engineers used concrete that possessed self-healing capabilities to build architecture and infrastructure, which still exists. Damage management is especially crucial for applications with limited access for maintenance or repair, ranging from medical applications,^[3] construction,^[4] aerospace,^[5,6] autonomous robotics,^[7] automotive and energy technology.^[8] Different methods of self-healing

approaches, especially in polymer science, have been proposed.^[3,9] However, finding practical ways for metals to self-heal that exceed microstructurally small fatigue cracks,^[10] especially in thin films, is still a relatively new field of research.

In the last decades, there has been a shift to flexible, stretchable, and bendable microelectronic devices. Wearable applications, sensors, or synthetic skin consist of multiple layers of thin films that must be designed to allow bending and stretching while conducting electricity. From the damage prevention side, different combinations of materials have been combined to generate functional multi-layered microelectronic concepts ranging from simply placing the brittle layer at the neutral axis^[11,12] to more complex criteria that show that the layer order is a crucial design parameter.^[13] Damage management solutions are still rare since flexible thin metal films pose different challenges as rigid bulk materials applications, like steel or concrete, which have space for capsules that store a healing agent. For flexible, thin metal films, capsule-based healing would be more complicated as it could lead to stress concentrations and high anisotropy. Therefore, the healing agent needs to be stored in a way that does not interfere with the damage prevention properties (optimally, even enhancing them) while providing management of the damage. Odom et al.^[14] solved this problem for metal inks, enabling autonomous healing using core-shell microcapsules in the substrate, which, if damaged, would dissolve the polymer binder of

C. O. W. Trost, A. Lassnig, P. Kreiml, M. J. Cordill
Erich Schmid Institute of Materials Science
Austrian Academy of Sciences
Jahnstrasse 12, Leoben, Styria 8700, Austria
E-mail: claus.trost@oeaw.ac.at; megan.cordill@oeaw.ac.at

A. Lassnig
Department of Materials Science & Engineering
University of California
170 Hearst Memorial Mining Building, Berkeley, California 94720, USA

P. Kreiml
Infineon Technologies Austria AG
Villach, Carinthia 9500, Austria

T. Jörg, V. L. Terziyska, C. Mitterer, M. J. Cordill
Department of Materials Science
Montanuniversität Leoben
Jahnstrasse 12, Leoben, Styria 8700, Austria

T. Jörg
Austria Technologie & Systemtechnik (AT&S) Aktiengesellschaft
Fabriksgasse 13, Leoben 8700, Styria, Austria

 The ORCID identification number(s) for the author(s) of this article can be found under <https://doi.org/10.1002/adma.202401007>

© 2024 The Authors. Advanced Materials published by Wiley-VCH GmbH. This is an open access article under the terms of the [Creative Commons Attribution](https://creativecommons.org/licenses/by/4.0/) License, which permits use, distribution and reproduction in any medium, provided the original work is properly cited.

DOI: 10.1002/adma.202401007

the used matrix, allowing the Ag particles to be mobile and redistribute, thus healing the crack.^[14] Ding et al.^[15] created thin-film transistor circuits with healing capabilities based on a dispersion of conductive particles in an insulating fluid. The particles align themselves at broken circuits due to the appearance of an electric field.^[15] Yurkevich et al.^[16] invented a rapid entropy-driven self-healing mechanism for metal oxides, enabling future use for transparent conductive metal oxides by storing their healing agent in the substrate and activation upon atmosphere exposure. For metal films, healing is even more limited as no mobile particles can easily be created. Putz et al.^[17] showed that electromigration can heal cracks of several nm wide in 50 nm thin Gold films on a flexible substrate.^[17] More recently, Danzi et al.^[18] investigated rapid self-healing of cracks up to 500 nm width on 100 nm thin films of Gold and Copper by using 50 nm Ni/Al bilayer films as a heat source, generating severe but rapid heat pulses to heal the material.^[18]

Molybdenum is a brittle material that finds widespread use in flexible devices such as solar cells,^[19–21] thin film transistors and liquid crystal displays.^[22–24] Mo is used due to its low electrical resistance, chemical inertness, high acoustic impedance, and high thermal stability.^[22,25,26] The Mo films are often the limiting factors when it comes to the flexibility of the devices. Therefore, Jörg et al.^[27–29] investigated the electro-mechanical properties of sputtered thin films made of pure Mo and Mo-alloys. For $\text{Mo}_{1-x}\text{Cu}_x$ alloys, they showed that the electro-mechanical properties, such as the deformation behavior, changed with increasing Cu content.^[29] Gao et al.^[30] investigated the mechanical and electrical properties of $\text{Mo}_{1-x}\text{Ag}_x$ over the entire composition range. They studied the system due to its superior hardness, decreased costs, and increased electrical erosive resistance performance compared to pure Ag.^[30,31] Sputtered $\text{Mo}_{1-x}\text{Ag}_x$ ($18 \leq x \leq 52.1$) films on flexible polymer substrates were found to exhibit self-formation of single crystal Ag nanoparticles at the surface, even at room temperature.^[32] The nanoparticles formation in the metastable Mo-Ag system is driven by phase-separation into polycrystals due to highly positive enthalpy of mixing (H_{mix}) that outweighs the enthalpy of segregation (H_{seg}) significantly.^[33,34] Due to the biocompatibility, hydrophilicity and particle formation of the $\text{Mo}_{1-x}\text{Ag}_x$ ($18 \leq x \leq 58.9$) system, it can be used to create an effective substrate for surface-enhanced Raman scattering.^[32,35–37] With high Ag contents (87 at%), the binary system is known to have strong light-trapping properties.^[38] Segregation of noble metals to surfaces has been used in “chameleon coatings” with different matrix materials such as Yttrium^[39] CrN^[40,41] or MoN.^[42] Such coatings are known for their favorable friction properties for high-temperature tribological aerospace applications.^[39] Hu et al.^[39] showed that by creating a multilayered architecture with 100 nm TiN diffusion barriers, the coating’s wear life could be increased, and the Ag diffusion could be controlled and directed.^[39]

Co-sputtered metastable $\text{Mo}_{1-x}\text{Ag}_x$ alloy films on Polyimide that combine damage prevention and damage management mechanisms were investigated within this work. Adding a capping layer as a barrier suppressed segregation until cracks emerged, which created an energetically favorable surface for diffusion. This suppression was checked by ageing the samples for several months at room temperature. The limits of the method were further investigated, showing that the method is

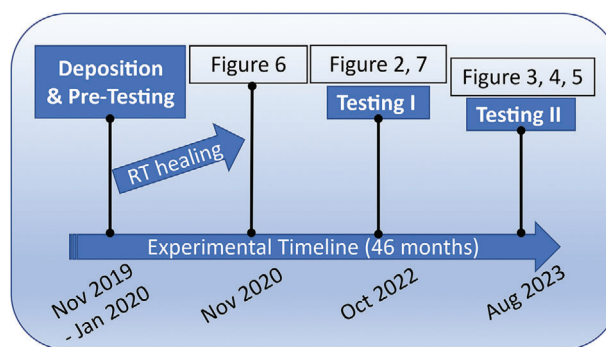


Figure 1. Timeline of the experimental progress.

autonomous intrinsic as defined by Zhang et al.^[1] but becomes more effective with increasing temperature. The healable crack width is in the regime of several hundred nanometers.

2. Results

2.1. Timeline

To accurately describe the presented long-time study (46 months), a timeline has to be introduced (Figure 1). The samples were deposited in November 2019 and directly pre-tested in the following weeks. This was followed by a room temperature annealing to distinguish strained and unstrained samples in terms of room temperature segregation behavior. In 2022 and 2023, the samples were checked for surface segregations, and two testing periods (Testing I and Testing II) were performed, resulting in different figures presented in this study.

2.2. Fractographic Analysis

Figure 2 shows a scanning electron microscopy (SEM) analysis of the sample morphologies, each consisting of a top view of a strained (1) and healed (strained and annealed) (2) sample and a cross-sectional focused ion beam (FIB) cut of a healed sample (3) after straining samples to 4%. Annealing was performed for 2 hrs. at 350 °C in a vacuum furnace. The self-healing is not directly apparent for $\text{Mo}_{82}\text{Ag}_{18}$. The unhealed (Figure 2a1) and healed surface (Figure 2a2) views show no distinct Ag segregations. The cross-section in Figure 2a3 reveals that the crack is partially filled, including where substrate damage has occurred, thereby connecting the crack flanks and decreasing resistance of the film. With increasing Ag content, the healing mechanism becomes more pronounced. Figure 2b2 shows that $\text{Mo}_{69}\text{Ag}_{31}$ surface segregations become evident after annealing. The cross-sectional image (Figure 2b3) shows that the crack is filled, and an Ag particle was produced at the top of the surface. In $\text{Mo}_{33}\text{Ag}_{67}$, presented in Figure 2c, the cracks are not straight as for films with lower Ag content, as cracks are shorter and meander through the material. The Ag particles only formed directly at the cracks (Figure 2c2), indicating that the rest of the capping layer remained intact and prevented the segregation even at elevated temperatures. The cross-sectional image in Figure 2c3 shows that the crack paths are completely healed, including substrate damage in the vicinity of the interface.

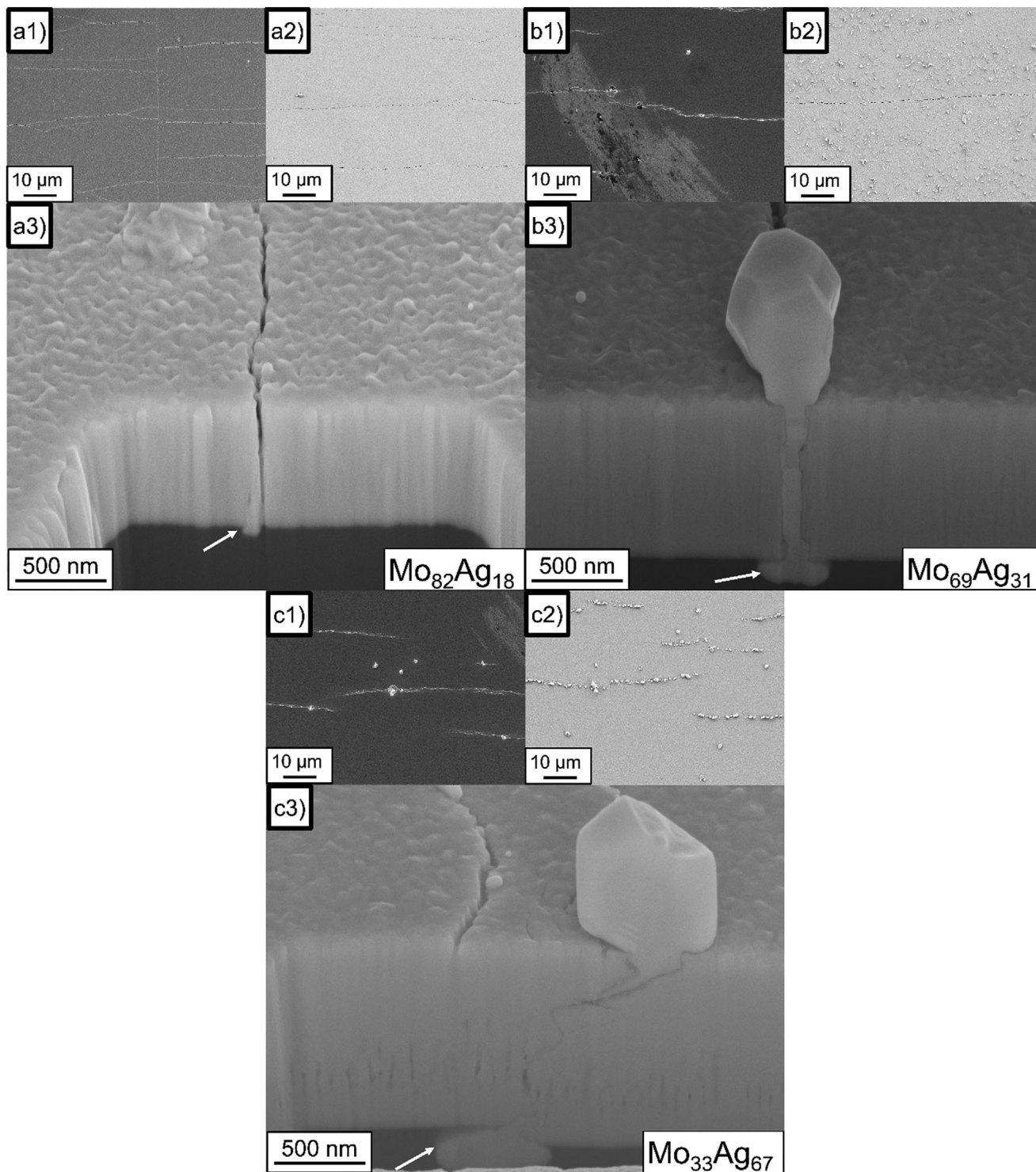


Figure 2. SEM images of samples strained to 4% strain for each Mo_{1-x}Ag_x composition being a) Mo₈₂Ag₁₈, b) Mo₆₉Ag₃₁, and c) Mo₃₃Ag₆₇, respectively. All sub-figures marked with 1) correspond to the relaxed state after cracking, 2) the annealed state (350 °C for 2 h), and 3) FIB cross-sections of annealed samples. The white arrows indicate where the healing agent fills up the substrate damage.

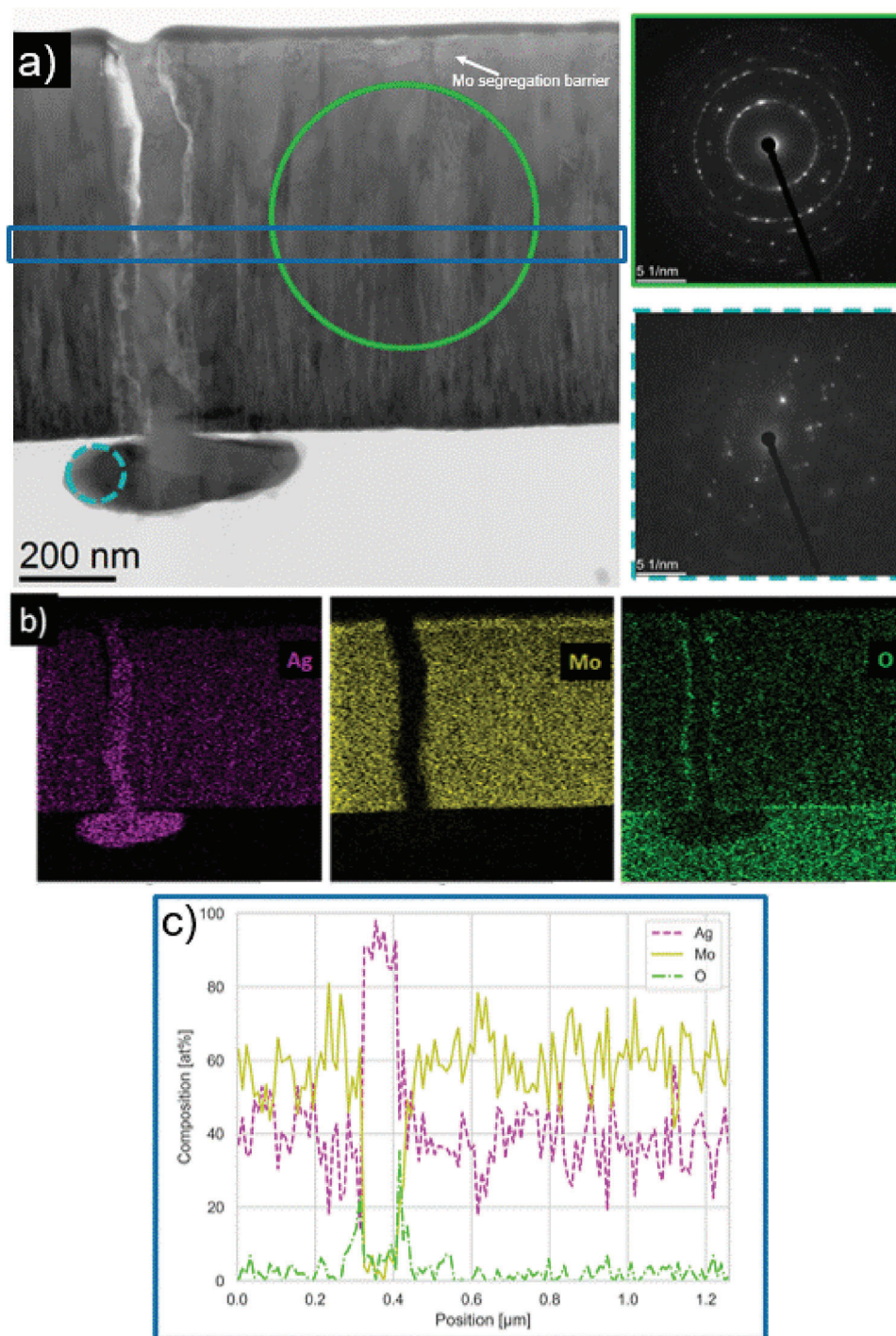


Figure 3. a) BF-STEM of the cross-sectional healed crack with selected area diffraction patterns of the Mo₆₉Ag₃₁ matrix (top right) and Ag filling (bottom right). The circles show the location and size of the selected area apertures using the same contours, respectively. b) elemental maps and c) line scans across the healed crack, as marked in a). (Color online).

Cross-sectional transmission electron microscopy (TEM) analysis was performed on a healed Mo₆₉Ag₃₁ sample to show that the crack was filled by Ag segregation. **Figure 3** presents a bright-field scanning transmission electron micrograph (BF-STEM) of the cross-section with the corresponding selected area diffraction (SAD) patterns of the Mo₆₉Ag₃₁ matrix and the healing agent

(Ag), respectively. The positions of the selected area apertures at which the diffraction patterns were taken are highlighted in the STEM micrograph. The SAD pattern of the Mo₆₉Ag₃₁ matrix confirms a body-centered cubic (BCC) structure with a lattice parameter of the dominant Mo ($a_{\text{Mo}} = 3.14 \text{ \AA}^{[43]}$). Elemental maps of the same cross-section were recorded using an energy-dispersive

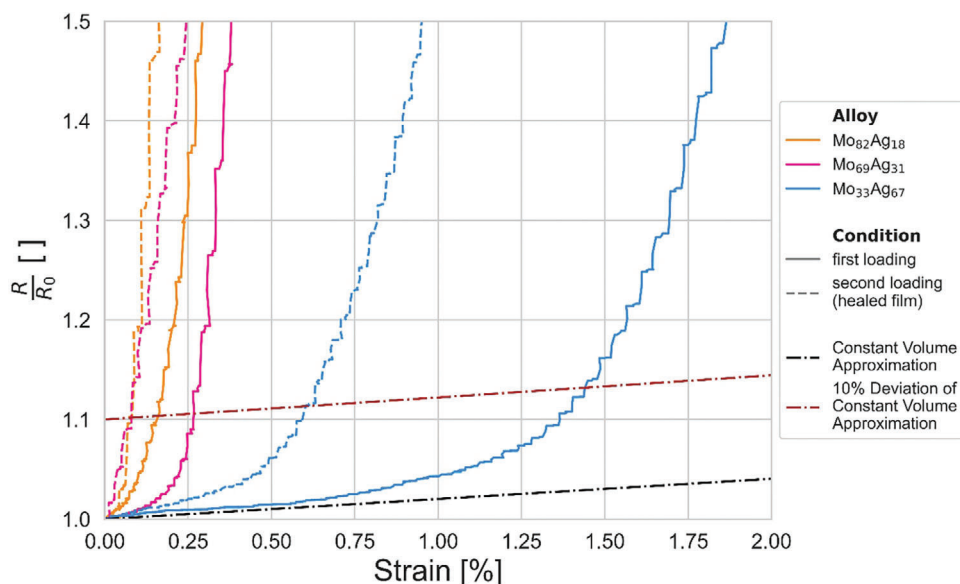


Figure 4. Evolution of the normalized resistance upon straining for different $\text{Mo}_{1-x}\text{Ag}_x$ alloys. The COS for an alloy is reached as soon as the point-dashed 10% deviation line from the constant volume approximation is crossed. Full lines represent the first loading to 4% strain, and dashed lines re-loading after straining and annealing treatment (healed state). Color online.

X-ray spectroscopy (EDX) detector, as shown in Figure 3b. This confirms that only Ag is present in the former crack and the damaged substrate. The Mo distribution map highlights the Mo capping layer. The Ag elemental map confirms the absence of Ag in the Mo capping layer after the annealing step, showing that it acts as an effective diffusion barrier. Figure 3c shows an elemental line scan across the healed structure, revealing an O enrichment in the crack walls ($\text{Mo}_{1-x}\text{Ag}_x$ -Ag interfaces) due to exposure to the atmosphere before the healing step.

2.3. Electro-Mechanical Characterization

All samples were aged at room temperature for several months, as visualized in Figure 1. During this period, hardly any silver particles were observed. For samples without the segregation barrier, surface segregation occurred on the entire surface during significantly less time at room temperature.^[36,44] All samples were strained to 4% and then annealed at 350 °C for 2 h to accelerate the self-healing. All samples exhibit significant cracking after applying 4% strain. The effect of strain on an electrical resistor can be described via the constant volume approximation.^[45] The constant volume approximation was used to define the behavior of an ideally stretched thin film before cracking occurs. It is defined as:

$$\frac{R}{R_0} = \left(\frac{L}{L_0} \right)^2 = (1 + \epsilon)^2 \quad (1)$$

where $\frac{R}{R_0}$ is the resistance (R) normalized by the initial resistance (R_0), $\frac{L}{L_0}$ is the gauge length (L) normalized by the initial gauge length (L_0) and ϵ is the strain. Cracking of the thin films will result in deviations from the constant volume approximation because the presence of through thickness cracks in the

film will significantly hinder conductivity in the film. As a result, a crack onset strain (COS), or the initial fracture strain of the film, can be defined by a 10% deviation from the theoretical behavior.^[27,46–48] This definition is commonly used to define the COS as it allows to compare the cracking of different films based on their electrical properties in a normalized way. The COS values depend on the material properties and thin film architecture (composition, thickness, residual stresses, and combination of brittle and ductile layers).^[29,48,49] The evolution of the normalized resistance and the COS for the investigated samples is shown in Figure 4 the 10% deviation from the theory is marked as an orange point dashed line. The COS for each experiment can be seen at the intersection between the different curves and the 10% deviation line. The COS values shift to higher values with increasing Ag content and film thickness. Upon re-straining of the already strained and healed samples, lower COS values were observed. For Mo-rich samples, the cracks nearly instantly reopened upon restraining (Figure 4b). For $\text{Mo}_{33}\text{Ag}_{67}$, the electro-mechanical properties are partially restored, and the healed cracks do not reopen immediately, as indicated by the intersection of the blue dashed line with the COS line.

Table 1 shows the evolution of the resistivity of samples in different states during an experimental cycle. Samples were first measured in their initial (aged) state. Note that the initial resistivity of the pristine $\text{Mo}_{1-x}\text{Ag}_x$ samples was found to be close to the values of the aged samples (within the error range reported in Table 1 for aged samples), which means that the pristine samples cannot be distinguished from the aged samples with the initial resistivity. All samples were strained to 4% strain, thereby cracking the films. After straining the substrates were allowed to relax. Due to the cracks induced into the films, the resistivities in the relaxed state were significantly higher (Table 1). Relaxing was followed by an annealing treatment to 350 °C for 2 h, thereby

Table 1. Resistivity of films strained to 4% in the as-deposited, relaxed and healed state. COS extracted from Figure 4 for films strained to 4% before and after healing. Saturation crack density at 15% strain was determined from pre-tests. Data combined with literature data for similar compositions extracted from Gao et al.^[30] using WebPlotDigitizer.^[53]

Composition	Resistivity [$\Omega \text{ m}$] $\times 10^{-8}$			COS [%]		Average Saturation Crack Density ρ_{crack} ($\epsilon = 15\%$) [μm^{-1}]	Literature Comparison	
	Initial - (aged)	Relaxed	Healed	Initial - (aged)	Healed		Composition	Resistivity [$\Omega \text{ m}$] $\times 10^{-8}$
Mo ₈₂ Ag ₁₈	230 ± 87	3907 ± 2331	557 ± 113	0.16	0.07	0.1 ± 0.002	Mo ₈₆ Ag ₁₄ [30]	140 ± 8
Mo ₆₉ Ag ₃₁	94 ± 2	631 ± 403	124 ± 34	0.27	0.07	0.11 ± 0.003	Mo ₆₆ Ag ₃₄ [30]	132 ± 9
Mo ₃₃ Ag ₆₇	61 ± 14	75 ± 7	55 ± 3	1.35	0.58	0.062 ± 0.003	Mo ₂₈ Ag ₇₂ [30]	55 ± 1

accelerating the healing process. After annealing, the resistivity dropped considerably compared to the relaxed state for all samples (Table 1). This decrease indicates that the crack flanks are reconnected, as shown in Figure 3, which allows current to flow again.^[50–52] Additional samples were strained to 15% (pre-tests), where the average saturation crack density was measured via the line intercept method and added to Table 1 to allow for quantitative comparison to other studies. Literature values of Gao et al.^[30] are shown in Table 1 to allow comparison between similar compositions with the presented work.

2.4. Additional Experiments

2.4.1. Constant Strain

A composition (Mo₆₉Ag₃₁) that led to straight cracks was chosen to be tested at constant strain. The cracks lead to significant increases in resistance, resulting in a network of cracks through the film and the capping layer. The sample had an initial resistance of 2 Ω . After cracking, 150 Ω were measured. The resistance was subsequently decreased to 3 Ω after annealing. Figure 5 shows that this procedure resulted in Ag segregation bridging a \approx 500 nm wide crack, even though the sample was kept in tension. Despite the surface segregations in Figure 2b2 (same composition and heat treatment), no surface segregations were observed in Figure 5, indicating less damage to the capping layer. The samples resistance was rechecked after additional ageing at room-temperature (12 months), which led to a further decrease in resistance to values of about 1 Ω .

2.4.2. Room Temperature Self-Healing

During pre-testing, samples were strained to 15%, thereby severely damaging the films and plastically deforming the sub-

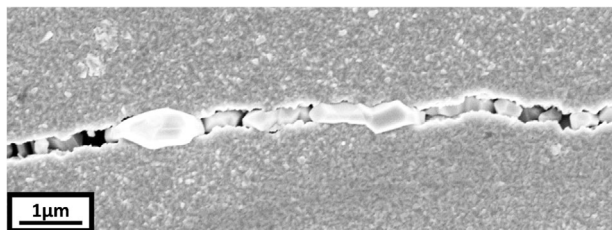


Figure 5. SEM micrograph of a Mo₆₉Ag₃₁ sample surface view. The sample was under strain during annealing and surface analysis to distinguish the substrate and sample effects.

strate. Afterward, they were cut in half, annealing one part while the other was stored at room temperature. Both sample parts were kept at approximately room temperature for 11 months, experiencing seasonal temperatures of 18 to 30 °C. In this period, cracks with an approximated width of 250 nm were healed in Mo₃₃Ag₆₇ (Figure 6b).

3. Discussion

3.1. Healing Mechanism

To trigger different healing mechanisms in thin films, specific conditions must be met, such as a high enough electric current to allow electromigration,^[17] a rapid exothermic reaction of parts of the multi-layered structure,^[18] or contact with the atmosphere.^[16] None of these external triggers are needed for the proposed healing mechanism, as it does not require external intervention for the healing process. Only ambient temperature and time are necessary to ensure atomic mobility for the Ag to diffuse into the crack. Thus, as defined by Zhang et al.,^[1] the healing mechanism can be classified as autonomous intrinsic. The effective atomic mobility is higher for Ag-rich alloys,^[54] this is evident from the room-temperature self-healing of Mo₃₃Ag₆₇ (Figure 6). The difference in mobility could possibly allow to tailor the self-healing behavior to the expected operating temperatures. The storage of the healing agent is achieved in a metastable Mo_{1-x}Ag_x interlayer encapsulated by a segregation barrier. The metastability is due to the positive mixing enthalpy for Mo and Ag over all possible compositions.^[54,55] Density Functional Theory (DFT) calculations and experimental data suggest that despite the positive enthalpy, Ag atoms tend to dissolve in the Mo lattice for sputter-deposited Mo-rich compositions, creating a BCC Mo-Ag metastable solid solution.^[30,54,56] Due to the combination of highly positive mixing enthalpy (H_{mix})^[34] and the low segregation enthalpy (H_{seg}) (positive for Mo-rich, negative for Ag-rich)^[34] for both the Mo-rich and Ag-rich alloys, the metastable alloy should decompose into separated polycrystals given enough temperature and time.^[33] The negative H_{seg} for Ag-rich alloys indicates that, as for Ni impurities in Cu,^[57] the solute (Mo) is even repelled from the grain boundary.^[34,57] The phase separation is shown by the polycrystalline Ag fillings of the cracks (Figure 3a), the surface segregations (Figure 2) and the homogeneous distribution of Ag inside Mo in the TEM-EDX image (Figure 3b). The uniform distribution of Ag in the matrix indicates the absence of grain boundary segregation, which would be present for classical nanostructured systems (Mo-Au) and duplex structures (Mo-Cr).^[33] No signs of grain boundary segregation were observed

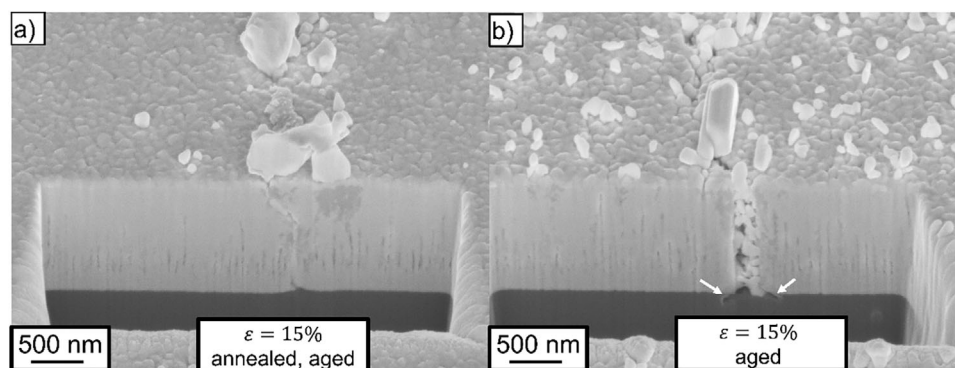


Figure 6. SEM micrographs of a Mo₃₃Ag₆₇ sample strained to 15% and a) annealed and aged 11 months at room temperature, b) aged 11 months at room temperature. White arrows mark the substrate damage.

(Figure 3b), which is evident as the energy reduction from phase separation significantly exceeds grain boundary segregation.^[58] Phase-separated polycrystals were not obtained inside the film, which indicates that more thermal activation would be needed to generate them, thus making cracks and damages of the segregation barrier favorable spots for Ag crystal nucleation and growth. Without a segregation barrier, the Ag of the presented Mo-rich metastable solid solution would segregate to the surface even at room temperature,^[32,36,44] resulting in surface particles made of single crystal Ag.^[32] The same applies for the cracks. The filling consisted of pure polycrystalline Ag (Figure 3b). The capping layer prevented surface segregations and stabilized the alloy for years at room temperature, as observed due to the lack of surface segregations in Figures 7 and 2. A similar effect on Ag depletion in Yttria Stabilized Zirconia YSZ–Ag–Mo nanocomposite coatings was discovered by Hu et al.^[39] YSZ–Ag–Mo can be used in high-temperature lubricating applications.^[39] Hu et al. showed that by adding TiN segregation barriers, no change in chemical composition was obtainable upon annealing to 500 °C, while Zirconia without barrier was Ag depleted.^[39]

The effectiveness of the mechanism comes into question. Since PI exhibits thermal shrinkage^[59–61] at elevated temperatures ($\Delta\epsilon_{th, U_{pilex-s} - 50\mu m} = 0.02\%$ at 200 °C for 2 h^[60]), experiments with constant strain during annealing (Figure 5) and room temperature annealing (Figure 6b) were performed, showing that the self-healing is still effective. When comparing Figure 6a,b, one can see that the crack flanks are pushed together when exposed to the annealing treatment, but the connection is still increased via the segregation into the crack. Figure 6b shows aged Mo₃₃Ag₆₇ with Ag particles filled cracks of ≈ 250 nm width at room temperature. Assuming that all cracks were of the same width and purely closed due to thermal shrinkage, the needed shrinkage to close the cracks ($\Delta\epsilon_{th, needed}$) can be calculated using:

$$\Delta\epsilon_{th, needed} = \rho_{crack} * width_{crack} * 100\% \quad (2)$$

where ρ_{crack} is the crack density and $width_{crack}$ the crack width, yielding 1.6% for the presented system (Mo₃₃Ag₆₇), significantly exceeding thermal shrinkage of PI reported in literature^[59–61] and further emphasizing that the healing is not only due to thermal shrinking.

The healed crack width in Figure 5 is in the same regime as reported by Danzi et al.,^[18] who healed cracks up to 500 nm, which is significantly more than Putz et al.,^[17] where cracks of several nm widths were healed using electromigration. The presented approach does not produce or rely on high temperatures, even for a short period, ensuring that the substrate material does not deteriorate, even locally. The experimental temperature of 350 °C, used to accelerate the healing process, is suitable, as temperatures above 500–800 °C for several hours would harm thin film-based devices and electronic circuits.^[18] Other healing mechanisms, such as electromigration-based healing, might deteriorate substrate properties locally depending on the polymer substrate thickness and glass transition temperature.^[62] It is unclear if the severe heating pulses produced in the samples of Danzi et al.^[18] would deteriorate the substrate's properties. In the presented system, healing occurs at room temperature, given enough time, as seen in Figure 6. Contrary to the cracks healed with increased temperature, the room temperature healed Ag-rich sample in Figure 6 did not show a complete filling of the substrate damage. The crack seemed filled with particles

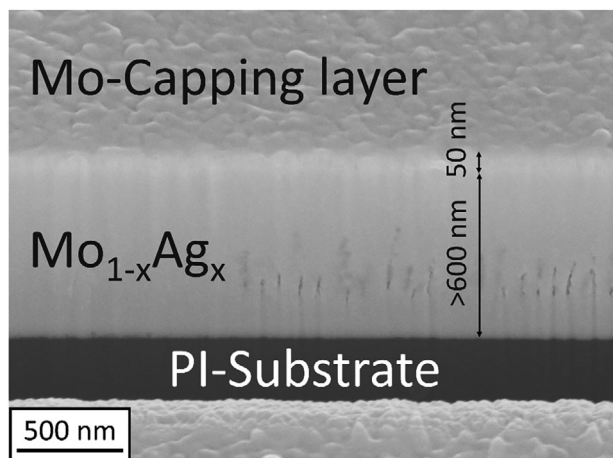


Figure 7. SEM micrograph of the investigated bilayer setup composed of a 50 μm thick polyimide (PI) substrate followed by a >600 nm thin Mo_{1-x}Ag_x layer and a ≈ 50 nm thin Mo capping layer. The shown image is an unstrained Mo₃₃Ag₆₇.

touching each other, still lacking thermal activation to merge into a full polycrystalline filling, as shown in the sample annealed at constant strain (Figure 5). The low-temperature healing is applicable for healing cracks in space applications as they exhibit temperature cycles of about -100 to $+100$ °C,^[63] temperatures in a good range for self-healing in a reasonable amount of time. Unlike Yurkevich et al.,^[16] no atmospheric exposure is needed to trigger the self-healing mechanism, making it a possible candidate material for space applications or inside multi-layered thin film systems.

3.2. Electro-Mechanical Behavior and Fractography

The resistivity of Mo films has been reported between 5×10^{-8} (close to bulk Mo) and 2000×10^{-8} Ω m,^[27,64–74] heavily depending on the deposition parameters,^[72] microstructure^[74] and annealing treatments.^[71] For alloyed Mo films, values from 20 to 98×10^{-8} Ω m have been reported for MoRe alloys^[28,75] and values up to 108×10^{-8} Ω m for MoCu films.^[76] Co-sputtered Mo_{1-x}Ag_x films were investigated by Gao et al.,^[30] and their resistivity ranged between 55×10^{-8} and 140×10^{-8} Ω m^[30] for the same composition range as presented in this work. The data has been combined in Table 1, allowing a comparison of the resistivity. The presented Mo₈₂Ag₁₈ films had a significantly higher resistivity ($\approx 200 \times 10^{-8}$ Ω m), and the Mo₆₉Ag₃₁ samples exhibited values below those reported by Gao et al.^[30] Even after straining and healing, the Mo₆₉Ag₃₁ films showed lower resistivity. The Ag-rich (Mo₃₃Ag₆₇) films showed nearly identical resistance to the values reported by Gao et al.^[30]

To ensure precise experimental conditions, all samples were annealed to 350 °C for 2 h after straining to increase the atomic mobility of the Ag. Annealing treatments have also been demonstrated to positively impact the resistivity of uncracked Mo thin films.^[71] Such an effect could be superimposed, but it does not diminish the significance of the self-healing of the cracks, as the self-healing at room temperature has a more significant impact than expected from a heat treatment.

After healing, Mo-rich samples showed limited restoration of the resistivity and only minimal further damage tolerance upon restraining (Table 1). This minimal tolerance is indicated by the sharp increase of resistance upon restraining in Figure 4. Contrarily, the Mo₃₃Ag₆₇ system exhibited a complete recovery of the resistivity upon annealing and additional limited damage tolerance upon restraining (Table 1 and Figure 4). This damage tolerance restores the functionality (limited flexibility while remaining conductive) rather than the initial microstructure, which is a typical property of self-healing materials, according to Hager et al.^[8]

The average saturation crack density at 15% strain (Table 1) for the Mo-rich films is in the same regime as for pure Mo films of similar thickness (500 nm) sputter-deposited at 500 W.^[27] The Ag-rich film resulted in a lower crack density similar to sputtering pure Mo with 4–10 kW.^[27] Further conclusions cannot be drawn as the crack density also depends on the thickness of the films.^[70] Shifting from a Mo-based system to an Ag-based system led to less straight, more irregular and deflected cracks with more zig-zag patterns (Figure 2). Similar changes were reported by Jörg et al.^[29] for alloying Mo with Cu.^[29] Such changes were

correlated to increased fracture toughness by Gruber et al.^[77] for Ta/Cu bilayer films.^[77] Change in crack patterns indicates that, in addition to the damage management properties, the damage prevention properties of the film change for Mo-based and Ag-based films.

3.3. Substrate Damage

The damage of the substrate is often ignored in the literature, which is reasonable as the system usually loses its functionality with severe cracking of the metal films. This is not the case in the presented system. Therefore, damage to the substrate becomes interesting.

Cheikh et al.^[78] and Douville et al.^[79] investigated the fracture of metal-coated polymers experimentally and via finite element simulations. Cheikh et al.^[78] investigated ethylene tetrafluoroethylene (ETFE) coated with ZnO thin films of different thicknesses. They showed that cracks in their ZnO thin films lead to stress concentrations in the substrate.^[78] These resulted in localized (“butterfly wing shaped”) plastic strain bands in the substrate. These bands were positioned right and left of the crack in the film (45 tilt with respect to the substrate surface).^[78] Douville et al.^[79] investigated the fracture of metal-coated Polydimethylsiloxane (PDMS). They showed that deformations and cracks formed in the polymer substrate at the cracks in the films.^[79] They manifest as concave deformations in the substrate with peaks around both sides, which matched their experimental profiles.^[79]

For the presented system, substrate damage is visible in the cross-sectional images (Figures 2, 3, and 6). The “butterfly wing shaped” stress concentrations, described by Cheik et al.,^[78] are closely resembled in the damage shown in Figure 6b. Concave deformations are present in the substrate at Ag-filled damage sites in Figures 2 and 3. Note that there is a severe difference in the size of the damage reported by Douville et al.^[79] The deviations can be explained by the differences in mechanical properties between ETFE ($E = 1$ GPa, $\sigma_y = 21$ MPa^[78]), PDMS ($E = 0.0038$ GPa^[79]) and the used PI (Upilex-S, $E = 8.7$ GPa, $\sigma_y = 147$ MPa^[13]). This underlines that further investigations are necessary to describe substrate damage induced by thin film cracking on PI. Additionally, for the presented system, the newly formed Ag/PI interface in the damaged region needs further investigation.

4. Conclusion

Metastable co-sputtered Mo_{1-x}Ag_x thin films showed improved damage prevention and management with increasing Ag content. An autonomous intrinsic self-healing mechanism was introduced, relying on the ratio of the highly positive Mixing Enthalpy (H_{mix}) of the binary alloy combined with a segregation barrier to promote deliberate local segregation of the healing agent inside cracks. The metastable alloy is known to produce surface segregation even at room temperature. By adding a segregation barrier, the alloy became stable for several years at room temperature, as the segregation barrier restricted energetically favorable surfaces or interfaces that could become segregation sinks of the healing agent. The novel self-healing mechanism can be

Table 2. Co-sputtering procedures for the different compositions. Thicknesses were measured on multiple samples with 3 measurements per FIB cuts and TEM images.

Composition	Thickness (including capping layer) [nm]	Current [A]		Ar pressure (Pa)	Deposition time [min]
		Mo (2 Targets)	Ag		
Mo ₈₂ Ag ₁₈	669 ± 9	0.35	0.05	0.38	8
Mo ₆₉ Ag ₃₁	872 ± 14	0.35	0.10	0.38	8
Mo ₃₃ Ag ₆₇	1070 ± 35	0.35	0.35	0.38	4

used for flexible thin film applications. It can be compared to capsule-based healing, but thin metastable films encapsulated with segregation barriers are used instead of a nanosized capsule. The mechanism can be used in multi-layered systems and space environments as it does not require external intervention or atmosphere to trigger. The Mo_{1-x}Ag_x system allows for future damage tolerant and damage management designs, resulting in more sustainable, longer-lasting, flexible microelectronic components.

5. Experimental Section

Film Characterization: Sample surfaces were characterized using a scanning electron microscope (SEM, LEO 1525 Zeiss Inc, Oberkochen, Germany). The thicknesses of the samples (Table 2) were measured from scanning electron images of the film cross-sections prepared by dual beam focused ion beam (FIB, LEO 1540XB Zeiss Inc, Oberkochen, Germany). A SEM (Zeiss Evo-50) with an Oxford Instruments INCA extension was used to determine the chemical composition via energy-dispersive X-ray spectroscopy (EDX).

A Mo₆₉Ag₃₁ sample strained to 4%, followed by an annealing treatment at 350 °C for 2 h, was selected for a site-specific FIB lift-out since the sample experienced full thickness cracks. The lift-out was carried out to study the healing mechanisms of the proposed architecture. It was conducted in a Zeiss Auriga dual beam workstation equipped with an OmniProbe micromanipulator and a gas injection system (GIS). Before cutting, the sample was protected using a W overlayer applied with the GIS to avoid Ga implantation in the specimen. An electron transparent lamella containing a healed crack was then prepared, where FIB cutting currents in the last polishing step were set at 50 pA with a 30 kV acceleration voltage. The lamella was immediately investigated in a JEOL 2200 FS transmission electron microscope (TEM) operating at 200 kV equipped with an Oxford Aztec Ultim Max TEM EDX detector to study the elemental composition of the matrix material and filling material, respectively. Note that TEM EDX was used as a semi-quantitative technique as it was used without a calibration standard. Therefore, the measured composition might not reflect the actual composition precisely, but it still allows for an accurate description of the severe differences due to segregation. After 3 weeks at room temperature, the same lamella was re-investigated in the TEM (STEM and EDX) to confirm that the healed structure remained stable.

Film Synthesis: Different Mo_{1-x}Ag_x alloys (Table 2) with 50 nm thick Mo segregation barriers (capping layers) were sputter deposited using a laboratory-scale unbalanced direct current dc magnetron sputtering device. The films were deposited onto 50 µm Polyimide (PI, Upilex-S) substrates. Before deposition, the PI substrates were cut using a Cricut Explore Air 2 into rectangular tensile specimen strips sized 6 × 50 mm. After cutting, the substrates were cleaned for 7 min with ethanol using an ultrasonic bath. The sputtering device was equipped with three circularly arranged AJA A320-XP magnetrons for 50.8-mm-diameter targets, which were focused onto a rotatable sample holder at a distance of 40 mm. The base pressure was ≤ 5 × 10⁻⁴ Pa. Before deposition, the substrates were

fixed with Kapton tape, followed by a plasma etching step. The etching was conducted for 120 s at an Ar pressure of 1.2 Pa in the chamber, using an asymmetrically bipolar pulsed dc plasma at -350 V with positive pulses set to +37 V and a frequency of 50 kHz. During co-sputtering of the Mo_{1-x}Ag_x films, two Mo targets were sputtered in current-controlled mode at 0.35 A (124 W), whereas the current at the one Ag target was varied to control the composition, see Table 2. The Argon working pressure was about 0.38 Pa. The 50 nm Mo segregation barriers were sputter deposited in power-controlled mode with 78 W for 86 s on top of the samples. No external heating was applied to the substrates, which were held at ground potential during film deposition. The accurate thickness of the segregation barrier was determined via a TEM image with 47 ± 3 nm. A SEM micrograph of the film architecture is shown in Figure 7.

Electro-Mechanical Characterization: Samples were strained to 4% engineering strain using an MTS Tytron 250 with isolated grips and a four-point setup connected to a Keithley 2000 multimeter. The electrical resistance was measured in situ as was performed by.^[27,74] The resistivity was calculated using:

$$\rho = \frac{R * t * w}{l} \quad (3)$$

where R is the electrical resistance, t is the film thickness, w is the sample width, and l is the length between contacts. The errors of the measurements were propagated. Afterwards, the samples were relaxed for several minutes, and the resistance was remeasured. The induced damage was quantified using SEM imaging. After characterization, an annealing procedure was performed at 350 °C for 2 h in a vacuum furnace. A heating rate of 10 K min⁻¹ was used, and the cooling was achieved significantly slower by switching off the furnace. The temperature was chosen as it is still lower than the detrimental temperatures (500–800 °C, for hours) for thin film applications.^[18] Polyimide can withstand 350 °C without degradation of the mechanical properties for significantly longer times.^[59,80–82] Furthermore, the 2 h were chosen since the procedure led to a significant amount of particles at the surface in pre-tests on samples without a capping layer.^[44] After the annealing step, the films were characterized by SEM, FIB and selected samples via TEM.

Pre-Testing: Pre-tests on strips were performed using an Anton Paar TS600 straining device that stopped at defined strains to allow for imaging of the film via confocal laser scanning microscopy (Olympus LEXT OLS4100). The saturation crack density was determined from images taken after relaxing from 15% strain via the line intercept method and three different lines per sample. The resistance of the samples was checked before and after straining, and the crack density was measured.

Constant Strain: To show that the resistance decrease after annealing is not purely due to a substrate effect, a Mo₆₉Ag₃₁ sample was strained and kept under strain to minimize the influence of substrate relaxation or thermal shrinking using a custom-made, manual straining device that allows the characterization of crack widths under strain. The sample in Figure 5 was strained until the resistance increased from 2 to 150 Ω. The increase in resistance was used to indicate damage, as the strain measurement on this custom-made device was unreliable. The strain was maintained during the heating treatment (350 °C for 2 h in a vacuum furnace), thereby minimizing the effect of the relaxing substrate.

Acknowledgements

The authors would like to thank Daniela Neumüller for her help with designing the graphics in the ToC. This work was in part supported by the Austrian Science Fund (FWF, Project No. I 4913-N) within the framework of the project Nanoarchitected films for unbreakable flexible electronics (NanoFilm) and project T891-N36. This work was also supported by the Austrian Research Promotion Agency [project number 857043].

Conflict of Interest

The authors declare no conflict of interest.

Data Availability Statement

The Python codes used to accurately work and merge the data of the MTS Tytron 250 with the electrical data measured by a Keithley 2000 multimeter will be published on GitHub (github.com/materialsguy). Further data will be shared upon reasonable request.

Keywords

flexible substrates, metastable alloy, MoAg, self-healing, thin films

Received: January 19, 2024

Revised: April 2, 2024

Published online:

- [1] S. Zhang, N. van Dijk, S. van der Zwaag, *Acta Metall. Sin. (Engl. Lett.)* **2020**, *33*, 1167.
- [2] L. M. Seymour, J. Maragh, P. Sabatini, M. Di Tommaso, J. C. Weaver, A. Masic, *Sci. Adv.* **2023**, *9*, eadd1602.
- [3] M. L. Del Prado-Audelo, I. H. Caballero-Florán, N. Mendoza-Muñoz, D. Giraldo-Gomez, J. Sharifi-Rad, J. K. Patra, M. González-Torres, B. Florán, H. Cortes, G. Leyva-Gómez, *Iran Polym. J* **2022**, *31*, 7.
- [4] M. R. Hossain, R. Sultana, M. M. Patwary, N. Khunga, P. Sharma, S. J. Shaker, *Environ. Chem. Lett.* **2022**, *20*, 1265.
- [5] L. Pernigoni, U. Lafont, A. M. Grande, *CEAS Space J.* **2021**, *13*, 341.
- [6] I. Levchenko, K. Bazaka, T. Belmonte, M. Keidar, S. Xu, *Adv. Mater.* **2018**, *30*, 1802201.
- [7] Y. J. Tan, G. J. Susanto, H. P. Anwar Ali, B. C. K. Tee, *Adv. Mater.* **2021**, *33*, 2002800.
- [8] M. D. Hager, P. Greil, C. Leyens, S. Zwaag, U. S. Schubert, *Adv. Mater.* **2010**, *22*, 5424.
- [9] S. Wang, M. W. Urban, *Nat. Rev. Mater.* **2020**, *5*, 562.
- [10] C. M. Barr, T. Duong, D. C. Bufford, Z. Milne, A. Molkeri, N. M. Heckman, D. P. Adams, A. Srivastava, K. Hattar, M. J. Demkowicz, B. L. Boyce, *Nature* **2023**.
- [11] S. Lee, J.-Y. Kwon, D. Yoon, H. Cho, J. You, Y. T. Kang, D. Choi, W. Hwang, *Nanoscale Res. Lett.* **2012**, *7*, 256.
- [12] S. Rathore, A. Singh, *Eng. Res. Express* **2020**, *2*, 015022.
- [13] M. J. Cordill, P. Kreiml, B. Putz, C. Trost, A. Lassnig, C. Mitterer, D. Faurie, P.-O. Renault, *Mater. Today Commun.* **2022**, *31*, 103455.
- [14] S. A. Odom, S. Chayanupatkul, B. J. Blaiszik, O. Zhao, A. C. Jackson, P. V. Braun, N. R. Sottos, S. R. White, J. S. Moore, *Adv. Mater.* **2012**, *24*, 2578.
- [15] L. Ding, P. Joshi, J. Macdonald, V. Parab, S. Sambandan, *Adv. Electron. Mater.* **2021**, *7*, 2001023.
- [16] O. Yurkevich, E. Modin, I. Šarić, M. Petravić, M. Knez, *Adv. Mater.* **2022**, *34*, 2202989.
- [17] B. Putz, O. Glushko, M. J. Cordill, *Mater. Res. Lett.* **2016**, *4*, 43.
- [18] S. Danzi, V. Schnabel, J. Gabl, A. Sologubenko, H. Galinski, R. Spolenak, *Adv. Mater. Technol.* **2019**, *4*, 1800468.
- [19] A. Bollero, M. Andrés, C. García, J. de Abajo, M. T. Gutiérrez, *phys. stat. sol. (a)* **2009**, *206*, 540.
- [20] M. Khan, M. Islam, A. Akram, Z. Qi, L. Li, *Mater. Sci. Semicond. Process.* **2014**, *27*, 343.
- [21] J. H. Scofield, A. Duda, D. Albin, B. L. Ballard, P. K. Predecki, *Thin Solid Films* **1995**, *260*, 26.
- [22] Y.-W. Yen, Y.-L. Kuo, J.-Y. Chen, C. Lee, C.-Y. Lee, *Thin Solid Films* **2007**, *515*, 7209.
- [23] T. Seo, T. Kim, Y. Seol, J. Choi, Flexible display and method of manufacturing the same.: U.S. Patent Application **2017**.
- [24] J. Heo, S. An, S. Bae, Flexible display apparatus and manufacturing method thereof. U.S. Patent Application No. 14/736, 893 **2017**.
- [25] R. Zhang, Z. Huo, X. Jiao, B. D. JieYang, H. Zhong, Y. Shi, *J. Nanosci. Nanotechnol.* **2016**, *16*, 8154.
- [26] S. Petroni, C. La Tegola, G. Caretto, A. Campa, A. Passaseo, M. de Vittorio, R. Cingolani, *Microelectron. Eng.* **2011**, *88*, 2372.
- [27] T. Jörg, M. J. Cordill, R. Franz, O. Glushko, J. Winkler, C. Mitterer, *Thin Solid Films* **2016**, *606*, 45.
- [28] T. Jörg, D. Music, F. Hauser, M. J. Cordill, R. Franz, H. Köstenbauer, J. Winkler, J. M. Schneider, C. Mitterer, *Sci. Rep.* **2017**, *7*, 7374.
- [29] T. Jörg, D. Music, M. J. Cordill, R. Franz, H. Köstenbauer, C. Linke, J. Winkler, J. M. Schneider, C. Mitterer, *Appl. Phys. Lett.* **2017**, *111*, 134101.
- [30] B. Gao, L. Zhou, C. Zhang, J. Zhu, L. Fu, W. Yang, D. Li, *Surf. Eng.* **2021**, *37*, 1143.
- [31] C.-H. Leung, H. Kim, *IEEE Trans. Comp., Hybrids, Manufact. Technol.* **1984**, *7*, 69.
- [32] X. Lian, Y. Lv, H. Sun, D. Hui, G. Wang, *Nanotechnology Reviews* **2020**, *9*, 751.
- [33] W. S. Cunningham, S. T. J. Mascarenhas, J. S. Riano, W. Wang, S. Hwang, K. Hattar, A. M. Hodge, J. R. Trelewicz, *Adv. Mater.* **2022**, *34*, 2200354.
- [34] H. A. Murdoch, C. A. Schuh, *J. Mater. Res.* **2013**, *28*, 2154.
- [35] H. Sun, X. Lian, Y. Lv, Y. Liu, C. Xu, J. Dai, Y. Wu, G. Wang, *Materials (Basel, Switzerland)* **2020**, *13*, 4205.
- [36] X. Lian, H. Sun, Y. Lv, G. Wang, *Mater. Lett.* **2020**, *275*, 128164.
- [37] D. Chen, Y. Li, L. Wang, Y. Wang, P. Ning, P. Shum, X. He, T. Fu, *Analyst* **2022**, *147*, 1385.
- [38] H. Sun, X. Lian, Y. Lv, G. Wang, *Opt. Mater. Express* **2021**, *11*, 1484.
- [39] J. J. Hu, C. Muratore, A. A. Voevodin, *Compos. Sci. Technol.* **2007**, *67*, 336.
- [40] K. Kutschej, C. Mitterer, C. P. Mulligan, D. Gall, *Adv. Eng. Mater.* **2006**, *8*, 1125.
- [41] C. P. Mulligan, D. Gall, *Surf. Coat. Technol.* **2005**, *200*, 1495.
- [42] X. Xu, J. Sun, F. Su, Z. Li, Y. Chen, Z. Xu, *Wear* **2022**, *488*, 204170.
- [43] W. P. Davey, *Phys. Rev.* **1925**, *25*, 753.
- [44] C. O. W. Trost, *Thermo-mechanical behaviour of Mo-Ag thin films* **2018**, <https://doi.org/10.34901/mul.pub.2023.271>.
- [45] N. Lu, X. Wang, Z. Suo, J. Vlassak, *Appl. Phys. Lett.* **2007**, *91*, 221909.
- [46] P. Kreiml, M. Rausch, V. L. Terziyska, H. Köstenbauer, J. Winkler, C. Mitterer, M. J. Cordill, *Thin Solid Films* **2018**, *665*, 131.
- [47] Y. Leterrier, L. Médico, F. Demarco, J.-A. Manson, U. Betz, M. F. Escolà, M. Kharrazi Olsson, F. Atamny, *Thin Solid Films* **2004**, *460*, 156.
- [48] S. Altaf Husain, P. Kreiml, C. Trost, D. Faurie, M. J. Cordill, P.-O. Renault, *Thin Solid Films* **2024**, *788*, 140173.
- [49] M. J. Cordill, P. Kreiml, C. Mitterer, *Materials (Basel, Switzerland)* **2022**, *15*, 926.
- [50] D. D. Gebhart, A. Krapf, C. Gammer, B. Merle, M. J. Cordill, *Scr. Mater.* **2022**, *212*, 114550.

- [51] D. D. Gebhart, A. Krapf, B. Merle, C. Gammer, M. J. Cordill, *J. Vac. Sci. Technol., A* **2023**, *41*, 023408.
- [52] M. J. Cordill, P. Kreiml, *Symp Digest of Tech Papers* **2021**, *52*, 111.
- [53] A. Rohatgi, Webplotdigitizer: Version 4.6, Pacifica, CA, USA, **2022**, <https://automeris.io/WebPlotDigitizer>.
- [54] K. Sarakinos, G. Greczynski, V. Elofsson, D. Magnfält, H. Högberg, B. Alling, *J. Appl. Phys.* **2016**, *119*, 95303.
- [55] C. Oses, E. Gossett, D. Hicks, F. Rose, M. J. Mehl, E. Perim, I. Takeuchi, S. Sanvito, M. Scheffler, Y. Lederer, O. Levy, C. Toher, S. Curtarolo, *J. Chem. Inf. Model.* **2018**, *58*, 2477.
- [56] G. Baolong, L. Deyi, Z. Jiajun, Y. Wulin, F. Licai, Z. Lingping, *Phys. B* **2021**, *602*, 412541.
- [57] S. M. Foiles, *Physical review. B, Condensed matter* **1989**, *40*, 11502.
- [58] T. Chookajorn, M. Park, C. A. Schuh, *J. Mater. Res.* **2015**, *30*, 151.
- [59] T. Park, D. A. Dillard, T. C. Ward, *J. Polym. Sci. B Polym. Phys.* **2000**, *38*, 3222.
- [60] UBE Corporation, Polyimide Business Department, UP-ILEX - Ultra heat-resistant films (Grade details) **2022**, ube.com/upilex/en/upilex_grade.html.
- [61] S. Heltzel, C. Semprimoschnig, M. van Eesbeek, *High Perform. Polym.* **2008**, *20*, 492.
- [62] D.-W. Jang, J.-H. Lee, A. Kim, S.-B. Lee, S.-G. Hong, *Sci. Rep.* **2017**, *7*, 12506.
- [63] I. Gouzman, E. Grossman, R. Verker, N. Atar, A. Bolker, N. Eliaz, *Adv. Mater.* **2019**, *31*, 1807738.
- [64] F. Keleş, Y. Atasoy, A. Seyhan, *Mater. Res. Express* **2019**, *6*, 126455.
- [65] G. Gordillo, F. Mesa, C. Calderón, *Braz. J. Phys.* **2006**, *36*, 982.
- [66] H. Rashid, K. S. Rahman, M. I. Hossain, A. A. Nasser, F. H. Alharbi, M. Akhtaruzzaman, N. Amin, *Results in Physics* **2019**, *14*, 102515.
- [67] F. Jingxue, W. Zhao, W. Wei, Y. Ye, Z. Lin, W. Xin, H. Ruijiang, S. Hui, M. Z. Q. Chen, *AIP Adv.* **2016**, *6*, 115210.
- [68] D. Rafaja, H. Köstenbauer, U. Mühle, C. Löffler, G. Schreiber, M. Kathrein, J. Winkler, *Thin Solid Films* **2013**, *528*, 42.
- [69] S.-F. Chen, S.-J. Wang, W.-D. Lee, M.-H. Chen, C.-N. Wei, H.-Y. Y. Bor, *AJMS* **2015**, *2*, 54.
- [70] T. Jörg, M. J. Cordill, R. Franz, C. Kirchlechner, D. M. Töbrens, J. Winkler, C. Mitterer, *Mater. Sci. Eng., A* **2017**, *697*, 17.
- [71] A. Marcelli, B. Spataro, S. Sarti, V. A. Dolgashev, S. Tantawi, D. A. Yeremian, Y. Higashi, R. Parodi, A. Notargiacomo, J. Xu, G. Cappuccio, G. Gatti, G. Cibin, *Surf. Coat. Technol.* **2015**, *261*, 391.
- [72] M. Kalaswad, J. O. Custer, S. Addamane, R. M. Khan, L. Jauregui, T. F. Babuska, A. Henriksen, F. W. DelRio, R. Dingreville, B. L. Boyce, D. P. Adams, *Integr. Mater. Manuf. Innov.* **2023**, *12*, 118.
- [73] N. Bansal, K. Pandey, K. Singh, B. C. Mohanty, *Vacuum* **2019**, *161*, 347.
- [74] M. J. Cordill, T. Jörg, O. Glushko, R. Franz, C. Mitterer, *Mater. Lett.* **2019**, *244*, 47.
- [75] J. Talvacchio, M. A. Janocko, J. Gregg, *J. Low Temp. Phys.* **1986**, *64*, 395.
- [76] A. G. Dirks, J. J. van den Broek, *J. Vac. Sci. Technol., A* **1985**, *3*, 2618.
- [77] P. A. Gruber, E. Arzt, R. Spolenak, *J. Mater. Res.* **2009**, *24*, 1906.
- [78] I. Ben Cheikh, G. Parry, D. Dalmas, R. Estevez, J. Marthelot, *Int. J. Solids Struct.* **2019**, *180*, 176.
- [79] N. J. Douville, Z. Li, S. Takayama, M. D. Thouless, *Soft Matter* **2011**, *7*, 6493.
- [80] M. Tsukiji, W. Bitoh, J. Enomoto, in *IEEE International Symposium on Electrical Insulation*, IEEE, Toronto, Canada, **1990**.
- [81] A. N. Hammoud, E. D. Baumann, E. Overton, I. T. Myers, J. L. Suthar, W. Khachen, J. R. Laghari, in *1992 Annual Report: Conference on Electrical Insulation and Dielectric Phenomena*, IEEE, New York, **1992**.
- [82] S. Heltzel, C. O. A. Semprimoschnig, *High Perform. Polym.* **2004**, *16*, 235.